Electronic Supplementary Material (ESI) for ChemComm.

Supporting Information for:

"Designing Ligand-Enhanced Optical Absorption of Thiolated Gold NanoClusters"

Luca Sementa[1], Giovanni Barcaro[1], Amala Dass[2], Mauro Stener[3,4,*] and Alessandro Fortunelli[1,*]

[1] *CNR-ICCOM & IPCF, Consiglio Nazionale delle Ricerche, via G. Moruzzi 1, 56124, Pisa, Italy*

[2] *Department of Chemistry and Biochemistry, University of Mississippi, 38677, Oxford (MS), USA*

[3] *Dipartimento di Scienze Chimiche e Farmaceutiche, Università di Trieste, via L. Giorgieri 1, I-34127, Trieste, Italy*

[4] *Consorzio Interuniversitario Nazionale per la Scienza e Tecnologia dei Materiali, INSTM, Unità di Trieste*

* Corresponding authors' emails: stener@univ.trieste.it; alessandro.fortunelli@cnr.it

Here we describe the procedure employed to derive the structures of the Au nanoclusters discussed in the main text and to simulate their excitation spectra, and we provide further details on the analysis of the TDDFT simulations in terms of independent-particle and fragment contributions and thermodynamic stability. For reasons of computational convenience, we used different codes to perform the structural and optical studies.

The geometry of the $[Au_{25}(SH)_{18}]^-$ complex was obtained by locally optimizing the structure taken from Ref. [1,17] within the S_6 symmetry framework. The NWChem software [2] was used in this calculation, adopting a Gaussian-type double-zeta basis set, a scalar-relativistic pseudo-potential describing the inner 60 electrons of gold [3,4], and the Perdew-Burke-Ernzerhof (PBE) exchange-correlation (xc-)functional [5]. Keeping the same point symmetry group, 12 H atoms were substituted by (i) 12 phenyl rings and (ii) 12 phenyl rings with *para*-NO_2 substituents and locally re-optimized using the same code and basis sets, thus producing relaxed geometries for $[Au_{25}(SPh)_{12}(SH)_6]^-$ and $[Au_{25}(SPh\text{-}pNO_2)_{12}(SH)_6]^-$ complexes. The location of the phenyl and phenyl-*para*-NO_2 substituents will be described below (see Fig. S4).

The geometries of the $[Au_{23}(SCH_3)_{16}]^-$, the $[Au_{23}(SPh)_{16}]^-$ and the $[Au_{23}(SPh\text{-}pNO_2)_{16}]^-$ complexes were obtained starting from the experimental structure of the $[Au_{23}(SC_6H_{11})_{16}]^-$ complex [6], substituting the SC_6H_{11} ligands with the (i) SCH_3, (ii) SPh, or (iii) SPh-*p*NO_2 ligands, respectively, and locally re-optimizing the structures. In these calculations the Plane-Wave QuantumEspresso software [7] was adopted in conjunction with ultra-soft pseudopotentials [8] and the PBE xc-functional [5], and a background positive charge was added to compensate for the negative charge of the species in periodic calculations. Values of 20 and 200 Ry were used as the cut-offs for the selection of the plane wave basis sets for describing the kinetic energy and the electronic density, respectively. For convenience of the reader, a schematic depiction of $[Au_{25}(SC_2H_4Ph)_{18}]^-$ and $[Au_{23}(SC_6H_{11})_{16}]^-$ clusters used as templates are depicted in Fig.S1(a,b).

A Scalar Relativistic Self-Consistent Field (SCF) Kohn-Sham (KS) formalism was employed to describe the cluster electronic structure at the Density Functional Theory (DFT) level. Relativistic effects were included at the Scalar-Relativistic Zeroth-Order Regular Approximation (ZORA) level [9] using the ADF suite of programs [10,11].

Optical spectra were calculated at the TDDFT level, which involves solving the following eigenvalue equation [12]:

$$\Omega \mathbf{F}_I = \omega_I^2 \mathbf{F}_I \quad (1)$$

where Ω is a four index matrix with elements $\Omega_{ia\sigma,jb\tau}$, the indices consisting of products of occupied-virtual (*ia* and *jb*) KS orbitals, while σ and τ refer to the spin variable. The eigenvalues ω_I^2 correspond to squared excitation energies while the oscillator strengths are extracted from the eigenvectors $\mathbf{F}_I$. The Ω-matrix elements can be formulated in terms of Kohn-Sham (KS) eigenvalues (ε) and the coupling matrix K (built employing the KS orbitals), in the present work the Adiabatic Local Density Approximation (ALDA) [13] for the xc-kernel has been employed.

The TDDFT calculations were performed at the optimized geometries, the scalar relativistic ZORA formalism was used, with the Frozen Core (FC) Polarized Triple Zeta (TZ2P) ZORA basis set of Slater Type Orbitals (STO) included in the ADF database for all atoms. The FC employed was up to 4f and 4p for Au, up to 2p for S and at 1s level for C, N and O. In the TDDFT calculations, the LB94 xc-functional was employed [14], which has the correct asymptotic 1/r long-range behaviour of the potential. Individual peaks were broadened with Gaussian functions of fwhm = 0.12 eV in all spectra. Absorption spectra reported in this work are always averages over the three *x,y,z* Cartesian components, i.e., they are obtained by summing the spectra produced by an electric field oriented along each of the three Cartesian directions and then dividing by 3: this should be taken into account for a proper comparison with literature results in which sometimes spectra are not divided by the factor 3.

The spectra reported in the main text were obtained by extracting a limited number of eigenvalues (roots) of the Casida matrix [12]. For example the spectrum of the $[Au_{23}(SPh\text{-}p NO_2)_{16}]^-$ in Fig.2(b) of the main text was obtained by extracting 700 roots. To test the numerical stability of the present calculations, in Fig.S2 we compare the spectrum of Fig.2(b) of the main text with a spectrum of the same compound obtained by extracting 850 roots of the Casida matrix. The excellent agreement between the two demonstrates that our spectra are fully converged.

In the main text, a $[Au_{25}(SH)_{18}]^-$ species has been taken as the starting point of our investigation as it represents the first model used to interpret the spectrum of the experimentally synthesized $[Au_{25}(SCH_2CH_2Ph)_{18}]^-$ compound. Use of more refined models such as $[Au_{25}(SCH_3)_{18}]^-$ do not change qualitatively our conclusions, as shown by Fig.S3 in which the

spectrum of $[Au_{25}(SCH_3)_{18}]^-$ obtained by using the present computational approach is reported for comparison.

For convenience of the reader and to provide a complete information on structure/optical-property relationships, in Fig.S4 we show atomistic depictions and optical spectra of all the species considered in Fig.1 of the main text.

To quantify the enhancement factor due to the resonance between the Au-S core motifs and the ligand fragments, it is useful to compare the optical spectrum of the final cluster with those of the separate fragment species, i.e.: $[Au_{23}(SPh\text{-}pNO_2)_{16}]^-$ with $[Au_{23}(SCH_3)_{16}]^-$ and [(HSPh-$pNO_2)_{16}$]. This is shown in Fig.S5, where the amplification due to interaction between separate excitations is apparent, as discussed in the main text.

Let us now provide more details on the optical spectrum of $[Au_{23}(SPh\text{-}pNO_2)_{16}]^-$ reported in Fig.2(b) of the main text and let us analyze this spectrum in terms of independent-particle contributions. Let us first recall that, in terms of electronic gap between the Highest-Occupied-Molecular-Orbital (HOMO) and Lowest-Unoccupied-Molecular-Orbital (LUMO), both the $[Au_{25}(SR)_{18}]^-$ and $[Au_{23}(SR)_{16}]^-$ compounds exhibit a large value, since they possess 8 nearly-free electrons which correspond to an electronic shell closure [6,15,17]. The variation of the HOMO-LUMO gap as a function of ligands' conjugating characteristics for $[Au_{25}(SR)_{18}]^-$ species has been studied in Ref. [20] and the decrease of such a gap for $[Au_{25}(SPh\text{-}pNO_2)_{18}]^-$ there predicted is in tune with our findings in Fig.2(b) of the main text: for example, the HOMO-LUMO gap of about 1.1 eV is consistent with the beginning of the optical spectrum in Fig.2(b). Let us analyze in more detail the spectrum of $[Au_{23}(SPh\text{-}pNO_2)_{16}]^-$ in Fig.2(b) of the main text. A tool that is particularly effective in identifying the emergence of plasmon resonances is the projection of TDDFT peaks onto the single-particle Kohn−Sham (KS) occupied/unoccupied pairs [22-24]. An analysis of the most intense absorption at 2.64 eV exhibiting an oscillator strength f=0.17 in the spectrum of Fig.2(b) of the main text shows that this absorption is made up of a mixture of many single-particle configurations, which is typical of plasmonic phenomena. The largest single-particle contributions to this excitation are:

21% ≡ 603 (30% S3p, 24% Au6s) -> 642 (43% O2p, 23%N2p, 15% C2p)

11% ≡ 604 (26% S3p, 30% Au6s) -> 643 (20% N2p, 38% O2p, 11% C2p)

with all other configurations contributing less than 7% each, where "603", "604", "642", etc. denote molecular orbitals, for which we also report in brackets the components projected onto the atoms in

the nanocluster distinguished by element. It is interesting to note that the occupied orbitals 603 and 604 are localized on the Au-S core motif, whereas the unoccupied orbitals 642 and 643 have strong components on the Ph-*p*NO_2 residues (C, N, and O atoms) in tune with the model discussed in Ref. [21]. As mentioned in the main text, the main difference between the intense optical band of $[Au_{23}(SPh\text{-}pNO_2)_{16}]^-$ and a typical plasmon resonance of larger metal nanoparticles consists in the fact that complex (many-body) electronic excitations do crowd in a narrow energy interval in the spectrum of $[Au_{23}(SPh\text{-}pNO_2)_{16}]^-$, albeit remaining separated, whereas in a fully developed plasmon resonance Coulomb interactions are strong enough to merge all these electronic states into a single collective excitation. This happens because the electronic excitations in the former are in part scattered over spatially separated ligands, so that the Coulomb interactions among them are correspondingly attenuated.

A more detailed comparison between TDDFT and KS spectra is reported in Fig.S6, in which we report for $[Au_{23}(SPh\text{-}pNO_2)_{16}]^-$ a comparison of interacting and non-interacting susceptibilities or between the TDDFT spectrum – taken from Fig.2(b) of the main text – and a spectrum calculated as KS eigenvalue differences and transition moments between molecular KS orbitals. One can notice the shift of the KS absorption band to higher energies in the TDDFT spectrum: from ≈1.8 to ≈2.6 eV [22-24]. It should also be added that the most intense KS single-particle peak at 1.88 eV with an oscillator strength $f = 1.14$ consists in a transition from the HOMO orbital (627), which has its main component on σ(Au-S) bonds with 30% Au 6s and 10% S 3p contributions, to the LUMO+17 orbital (645) which retains a σ*(Au-S) character but with different 43% Au 6s and 5% S 3p contributions: in the KS description the absorption happens mostly within the Au-S core motif, whereas, according to the TDDFT approach, response phenomena strongly involve ligands orbitals, including significant components on the more electronegative N and O atoms.

Finally, although the focus of the present work is to understand electronic spectra of ultra-small coated metal clusters and how to tune the ligands to obtain specific effects – so that we are less concerned here with synthesis protocols etc. –, we can ask in general whether these predictions are realizable and consistent with available experimental information.

From a structural point of view, for the transition from $[Au_{25}(SR)_{18}]^-$ to $[Au_{23}(SR)_{16}]^-$ to occur and be thermodynamically favorable, the R groups should exhibit appropriate sterically hindered geometrical features [6,15]. Steric hindrance of the organic R groups should be larger than in the slim R=C_2H_4Ph (phenyl-ethyl) group, as it happens in R=C_6H_{11} (cyclohexyl) or in the even

bulkier R=$C_{10}H_{15}$ (adamantyl) groups. Experimentally, it is proven that $[Au_{23}(SC_6H_{11})_{16}]^-$ (with a counter-ion) [6] and $Au_{24}(SC_{10}H_{15})_{16}$ (neutral) [15] can be crystallized. When R=adamantyl, a mixture of $Au_{23,24,25}(SC_{10}H_{15})_{16}$ compounds is actually produced [15], and it has been suggested [15] that this should also occur for R=cyclohexyl, while theoretical considerations indicate that favoring one given stoichiometry with respect to another also depends on environmental variables [15]. The R=Ph or R=Ph-*p*NO_2 groups here considered are reasonable candidates, and the corresponding nanoclusters should possess sufficient thermodynamic stability to be synthesized and used in practice. The steric hindrance of the R=Ph or R= Ph-*p*NO_2 groups is however inferior to that of R=C_6H_{11} and thus sub-optimal. The addition of one or two methyl substituents on the phenyl ring in ortho positions (which should not alter significantly the cluster electronic response) can increase the bulkiness of the R=Ph-*p*NO_2 group. To prove this, we have constructed a R=$\Re$=Ph-(*o*CH_3)$_2$-*p*NO_2 residue by adding two methyl groups on the phenyl ring in *ortho* positions while still keeping the NO_2 group in the *para* position, and studied the energetics of the following three species: $[Au_{25}(S\Re)_{18}]^-$, $[Au_{25}(S\Re)_{16}]^-$, and $[Au_{23}(S\Re)_{16}]^-$. Their geometries were generated via local relaxations starting from homologous structures containing adamantyl residues taken from Ref. [15]. As in Ref. [15], we can analyze the total formation energy (TFE) of these Au nanoclusters, defined as the energy of the reaction:

$$N\,Au + M\,RSH \rightarrow Au_N(SR)_M + M/2\,H_2 \qquad (1)$$

finding the following results (in Rydberg, Ry, units of energy):

$TFE[Au_{25}(S\Re)_{18}]^- = -5.21$ Ry
$TFE[Au_{25}(S\Re)_{16}]^- = -5.25$ Ry
$TFE[Au_{23}(S\Re)_{16}]^- = -4.93$ Ry

These numbers closely parallel those of the corresponding species containing adamantyl ligands from Ref.[15]:

$TFE[Au_{25}(SAdm)_{18}]^- = -5.19$ Ry
$TFE[Au_{25}(SAdm)_{16}]^- = -5.23$ Ry
$TFE[Au_{23}(SAdm)_{16}]^- = -4.89$ Ry

This proves two important points:

- the steric hindrance of the S$\Re$=SPh-(*o*CH_3)$_2$-*p*NO_2 ligand is very similar to that of the SR=SAdm ligand, thus it should be possible to synthesize both $[Au_{23,25}(S\Re)_{16}]^-$ and $Au_{24}(S\Re)_{16}$ (it can also be expected by analogy that placing only one methyl substituent in ortho position one should obtain an intermediate steric hindrance, similar to that of R=C_6H_{11});

- π-electron conjugation in the ligands does not affect significantly the thermodynamic stability of these species which is dominated by structural effects [25] – such as the bulkiness and rigidity of the ligands – rather than electronic conjugation.

Finally, to test the sensitivity of our computational approach to the choice of the xc-functional, in Fig.S7 the results of TDDFT calculations in which the PBE xc-functional instead of the LB94 xc-functional was employed to predict the optical spectrum of the separate species: $[Au_{23}$(SPh-*p*$NO_2)_{16}]^-$, $[Au_{23}(SCH_3)_{16}]^-$, and [(HSPh-*p*$NO_2)_{16}$], are reported. A comparison with Fig.S5 shows that the main features of the resonance enhancement phenomenon described in this work remain qualitatively the same.

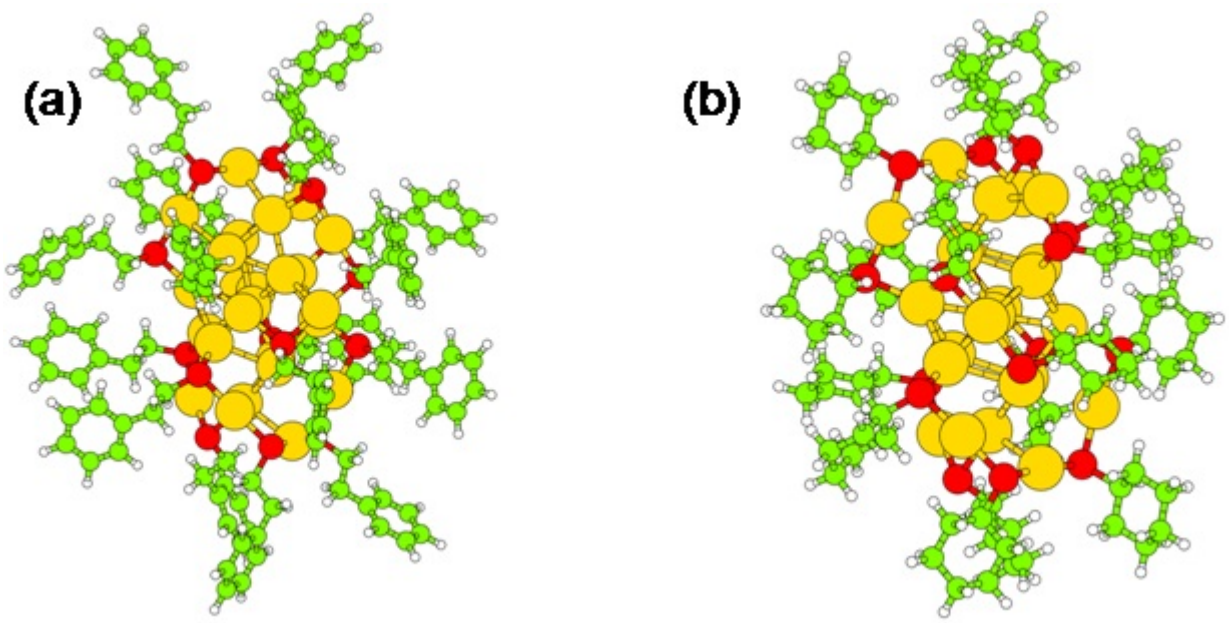

Figure S1. Schematic depiction of the clusters used as templates in the present work: (a) $[Au_{25}(SC_2H_4Ph)_{18}]^-$, (b) $[Au_{23}(SC_6H_{11})_{16}]^-$ compounds. Color coding: Au in yellow, S in red, C in green and H in gray. Coordinates taken from Refs. [1,15-17].

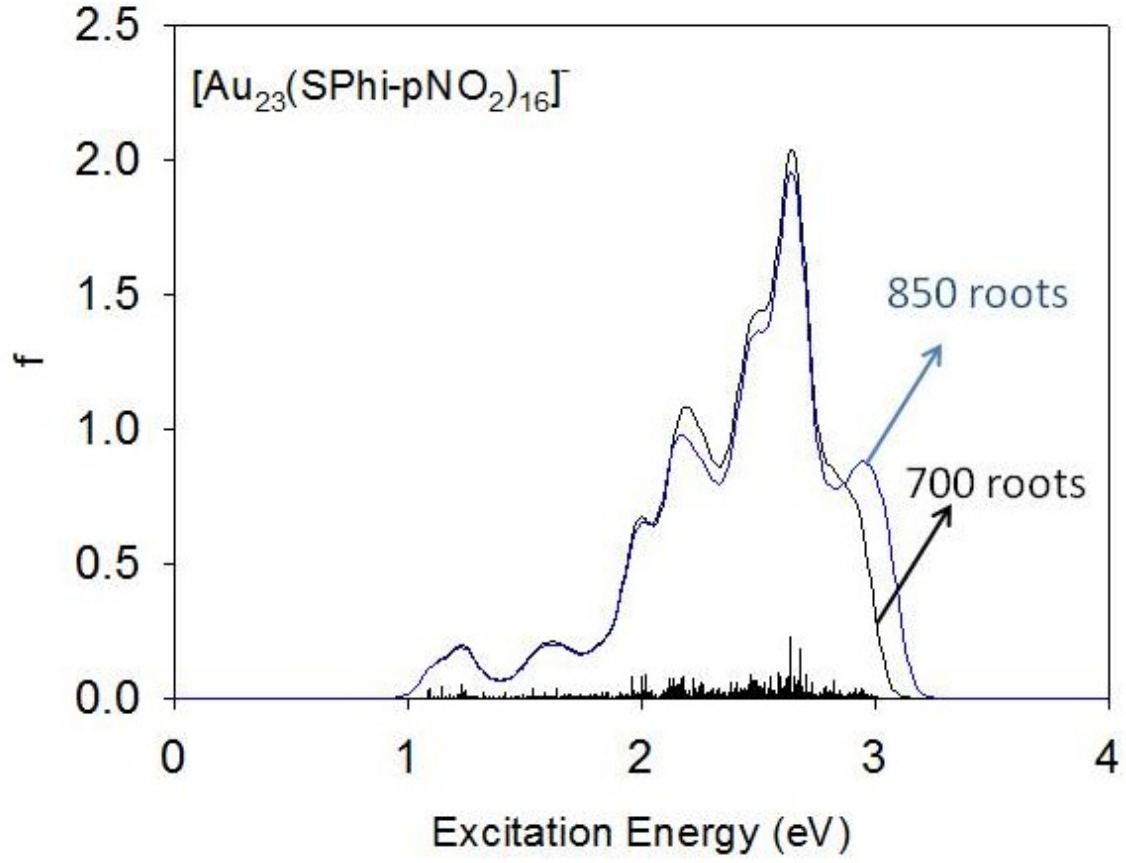

Figure S2. Comparison between the TDDFT spectra of $[Au_{23}(SPh\text{-}pNO_2)_{16}]^-$ obtained by extracting 700 or 850 roots of the Casida matrix, respectively.

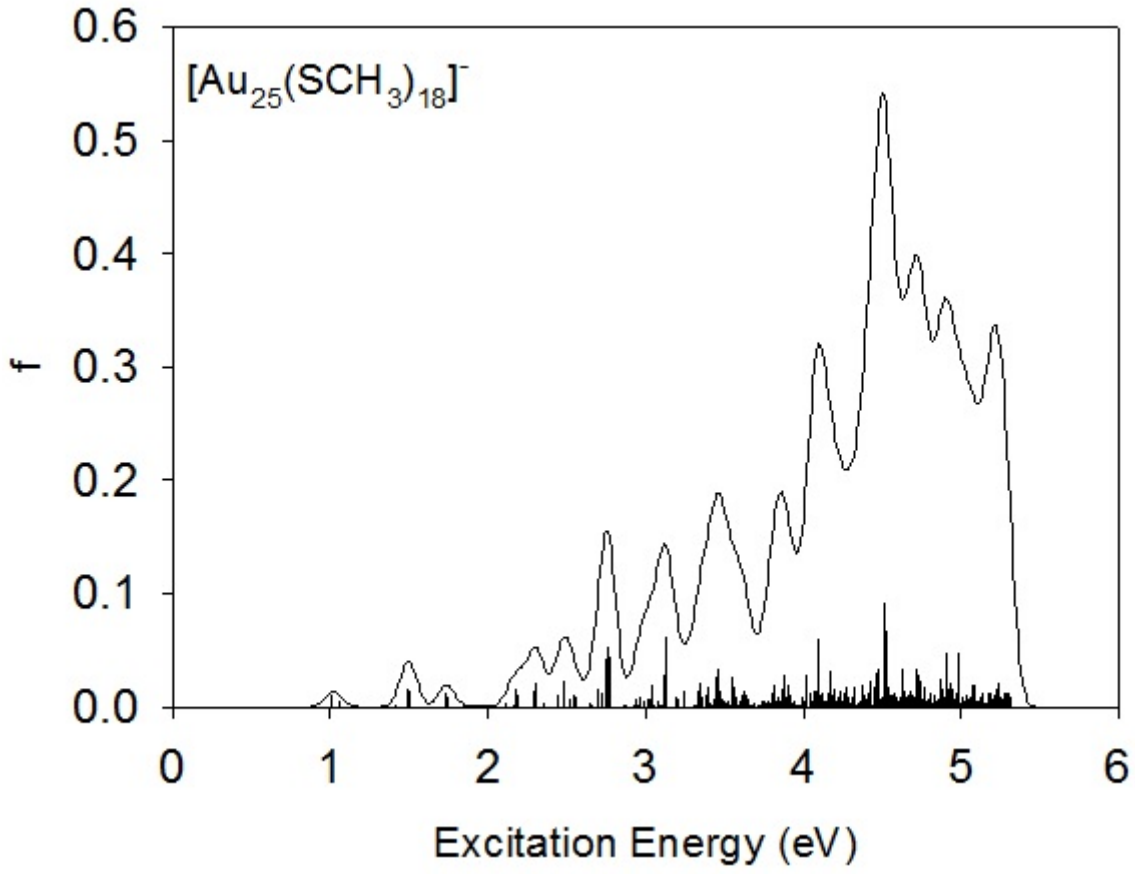

Figure S3. TDDFT simulated spectrum of $[Au_{25}(SCH_3)_{18}]^-$.

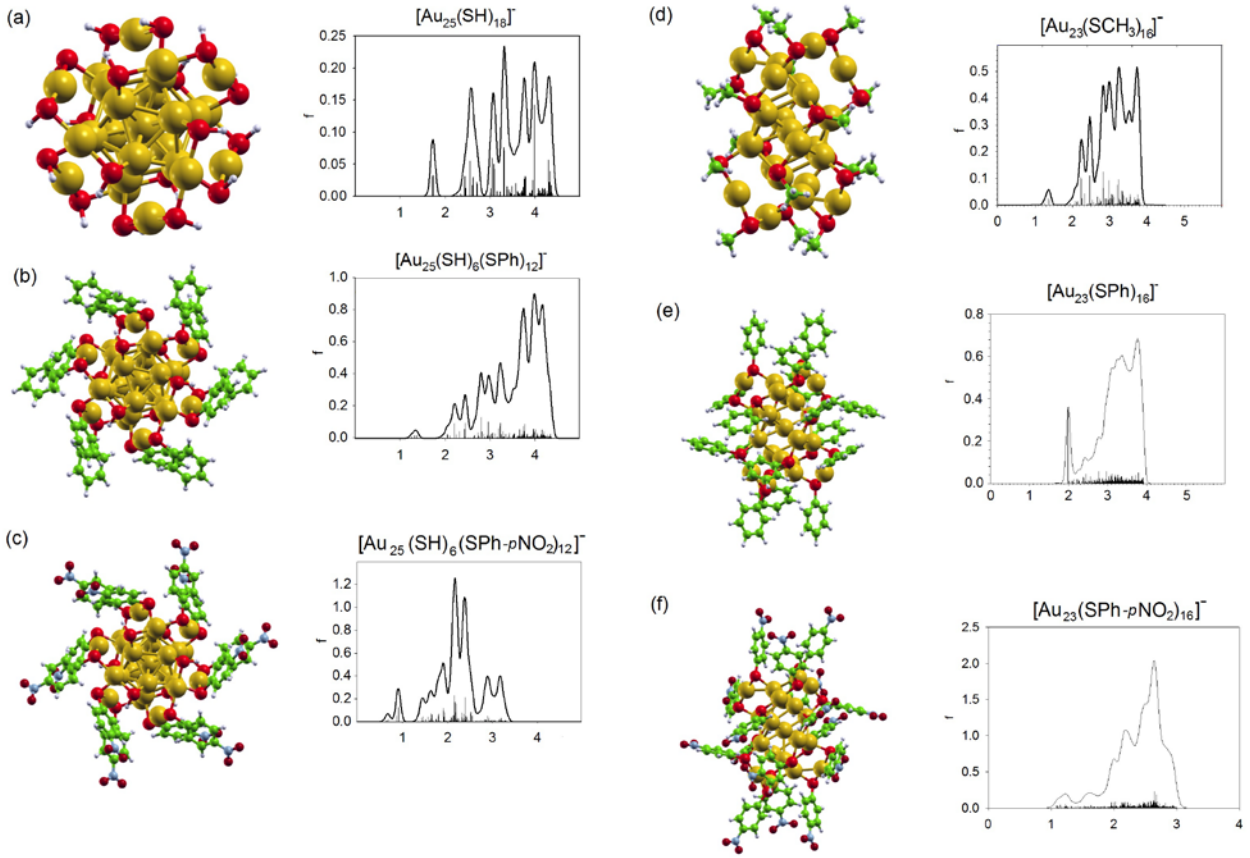

Figure S4. Schematic atomistic depictions and TDDFT simulated spectra of the species considered in the present work. Color coding: Au in yellow, S in red, C in green, H in gray, N in light blue, O in darker red (smaller spheres).

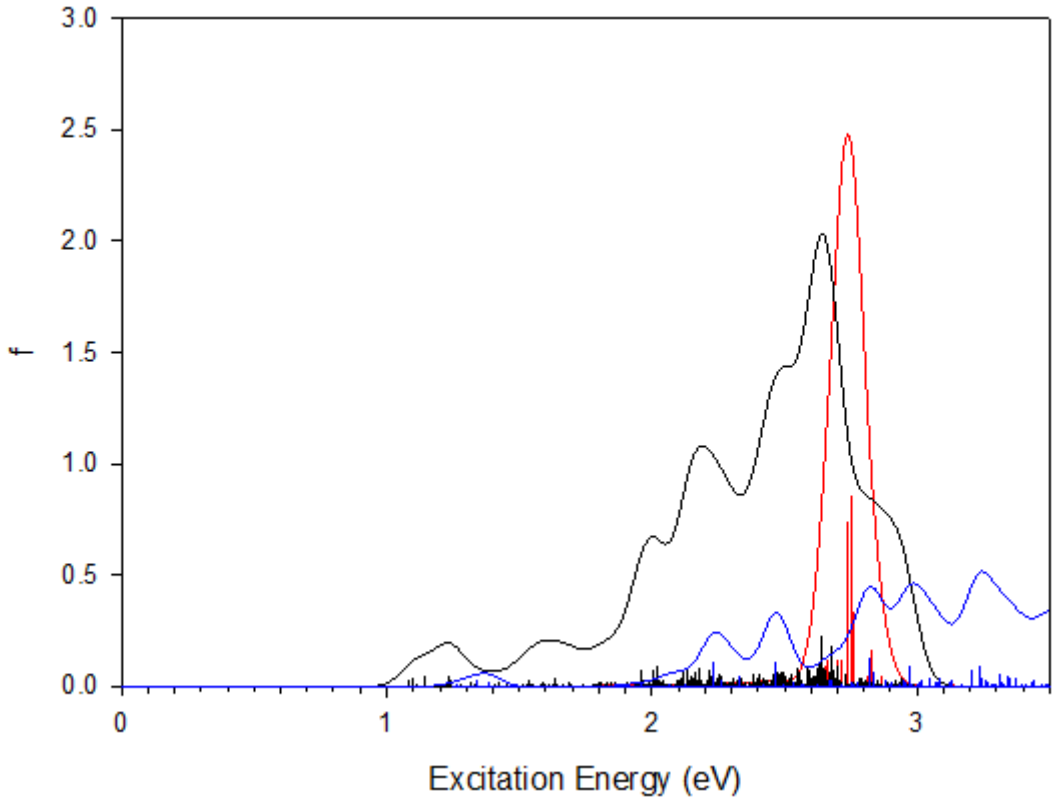

Figure S5. Comparison of the TDDFT optical spectra of: $[Au_{23}(SPh\text{-}pNO_2)_{16}]^-$ (black curve), $[Au_{23}(SCH_3)_{16}]^-$ (blue curve), and $[(HSPh\text{-}pNO_2)_{16}]$ (red curve) species, pictorially showing the enhancement due to resonance between Au-S core motif and ligand fragments.

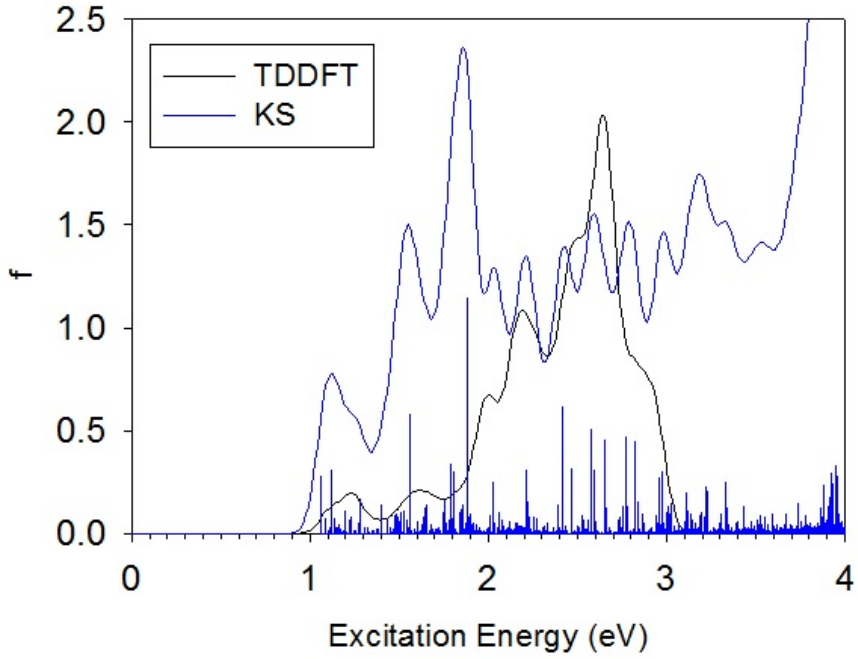

Figure S6. Comparison between the TDDFT spectrum (black) and a spectrum calculated as KS eigenvalue difference and transition moment between molecular KS orbitals (blue) of $[Au_{23}(SPh\text{-}p NO_2)_{16}]^-$. For the KS spectrum, individual transitions are also explicitly indicated as bars.

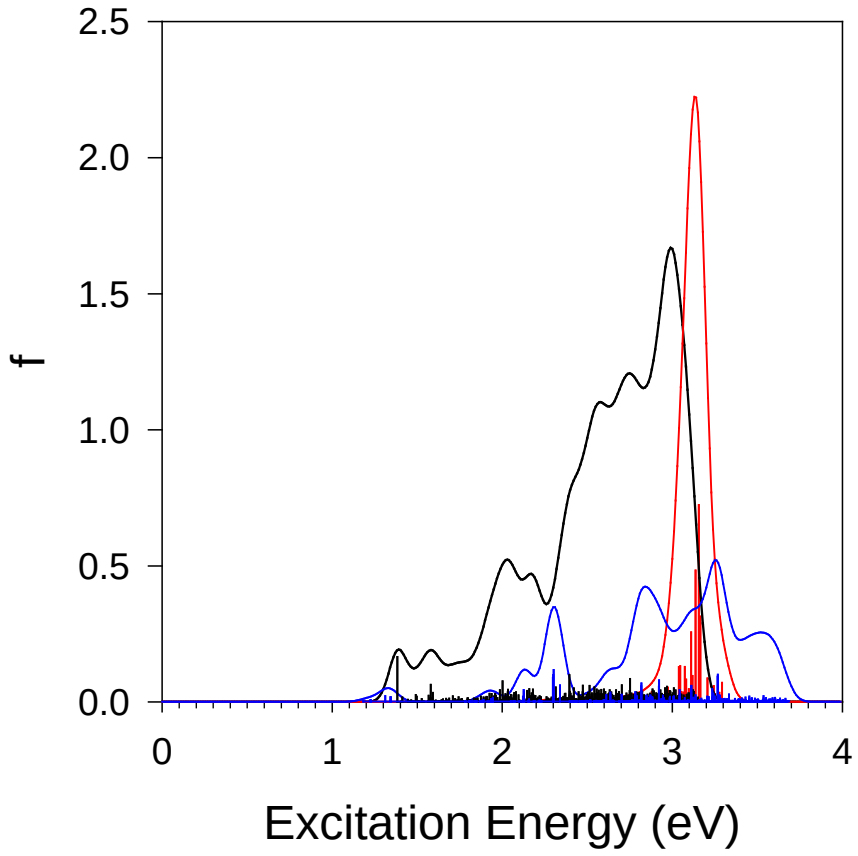

Figure S7. Comparison of the TDDFT optical spectra of: $[Au_{23}(SPh\text{-}pNO_2)_{16}]^-$ (black curve), $[Au_{23}(SCH_3)_{16}]^-$ (blue curve), and $[(HSPh\text{-}pNO_2)_{16}]$ (red curve) species calculated employing the PBE rather than LB94 as in Fig. S5) xc-functional. This figure pictorially shows that the enhancement due to resonance between Au-S core motif and ligand fragments remain qualitatively the same.

References

[1] Heaven, M. W.; Dass, A.; White, P. S.; Holt, K. M.; Murray, R. W. Crystal Structure of the Gold Nanoparticle [$N(C_8H_{17})4$][$Au_{25}(SCH_2CH_2Ph)_{18}$], *J. Am. Chem. Soc.* **2008**, *130*, 3754–3755

[2] Valiev, M.; Bylaska, E.J.; Govind, N.; Kowalski, K.; Straatsma, T.P.; van Dam, H.J.J.; Wang, D.; Nieplocha, J.; Apra, E.; Windus, T.L.; de Jong, W.A. NWChem: A comprehensive and scalable open-source solution for large scale molecular simulations, *Comput. Phys. Commun.* **2010**, *181*, 1477–1489

[3] Schaefer, A.; Huber, C.; Ahlrichs, R. Fully optimized contracted Gaussian basis sets of triple zeta valence quality for atoms Li to Kr, *J. Chem. Phys.* **1994**, *100*, 5829–5835

[4] Andrae, D; Haussermann, U.; Dolg, M.; Stoll, H.; Preuss, H. Energy-adjusted ab initio pseudopotentials for the second and third row transition elements, *Theor Chim Acta* **1990**, *77*, 123–141

[5] Perdew, J. P.; Burke, K.; Ernzerhof, M. Generalized Gradient Approximation Made Simple, *Phys. Rev. Lett.* **1996**, *77*, 3865-3868

[6] Das, A.; Li, T.; Nobusada, K.; Zeng, C.; Rosi, N. L.; Jin, R. Nonsuperatomic [$Au_{23}(SC_6H_{11})_{16}$]$^-$ Nanocluster Featuring Bipyramidal Au_{15} Kernel and Trimeric $Au_3(SR)_4$ Motif, *J. Am. Chem. Soc.* **2013**, *135*, 18264–18267

[7] Giannozzi, P.; Baroni, S.; Bonini, N.; Calandra, M.; Car, R.; Cavazzoni, C.; Ceresoli, D.; Chiarotti, G.L.; Cococcioni, M.; Dabo, I.; Dal Corso, A.; de Gironcoli, S.; Fabris, S.; Fratesi, G.; Gebauer, R.; Gerstmann, U.; Gougoussis, C.; Kokalj, A.; Lazzeri, M.; Martin-Samos, L.; Marzari, N.; Mauri, F.; Mazzarello, R.; Paolini, S.; Pasquarello, A.; Paulatto, L.; Sbraccia, C.; Scandolo S.; Sclauzero, G.; Seitsonen, A.P.; Smogunov, A.; Umari, P.; Wentzcovitch, R.M. QUANTUM ESPRESSO: a modular and open-source software project for quantum simulations of materials, *J. Phys.: Condens. Matter* **2009**, *21*, 395502

[8] Vanderbilt, D. Soft self-consistent pseudopotentials in a generalized eigenvalue formalism, *Phys. Rev. B* 1990, *41*, 7892

[9] van Lenthe, E.; Baerends, E. J.; Snijders, J. G. Relativistic regular two‐component Hamiltonians. *J. Chem. Phys.* **1993**, *99*, 4597–4610]

[10] Baerends, E. J.; Ellis, D. E.; Ros, P. Self-consistent molecular Hartree—Fock—Slater calculations I. The computational procedure. *Chem. Phys.* **1973**, *2*, 41-51

[11] Fonseca Guerra, C.; Snijders, J. G.; te Velde, G.; Baerends, E. J. Towards an order-N DFT method. *Theor. Chem. Acc.* **1998**, *99*, 391–403

[12] Casida, M. E. in “Recent Advances in Density-Functional Methods”; Chong, D. P., ed.; World Scientific: Singapore, 1995; p 155

[13] Gross, E. K. U.; Kohn, W. Time-Dependent Density-Functional Theory. *Adv. Quantum. Chem*. **1990**, *21*, 255–291

[14] van Leeuwen, R.; Baerends E. J. Exchange-correlation potential with correct asymptotic behavior. *Phys. Rev. A* **1994**, *49*, 2421–2431

[15] Crasto, D.; Barcaro, G.; Stener, M.; Sementa, L; Fortunelli, A.; Dass, A. $Au_{24}(SAdm)_{16}$ Nanomolecules: X‑ray Crystal Structure, Theoretical Analysis, Adaptability of Adamantane Ligands to Form $Au_{23}(SAdm)_{16}$ and $Au_{25}(SAdm)_{16}$, and Its Relation to $Au_{25}(SR)_{18}$ *J. Am. Chem. Soc.* **2014**, *136*, 14933−14940

[16] Zhu, M.; Aikens, C.M.; Hollander, F.J.; Schatz, G.C.; Jin, R. Correlating the Crystal Structure of A Thiol-Protected Au_{25} Cluster and Optical Properties *J. Am. Chem. Soc.* **2008**, *130*, 5883–5885

[17] Akola, J.; Walter, M.; Whetten, R. L.; Häkkinen, H.; Grönbeck, H. On the Structure of Thiolate-Protected Au_{25} *J. Am. Chem. Soc.* **2008**, *130*, 3756–3757

[18] Aikens, C. M. Effects of Core Distances, Solvent, Ligand, and Level of Theory on the TDDFT Optical Absorption Spectrum of the Thiolate-Protected Au25 Nanoparticle *J. Phys. Chem. A* **2009,** *113*, 10811–10817

[19] Aikens, C. M. Geometric and Electronic Structure of $Au_{25}(SPhX)_{18}^-$ (X = H, F, Cl, Br, CH_3, and OCH_3) *J. Phys. Chem. Lett.* **2010,** *1,* 2594– 2599

[20] Tlahuice-Flores, A.; Whetten, R. L.; Jose-Yacaman, M. Ligand Effects on the Structure and the Electronic Optical Properties of Anionic $Au_{25}(SR)_{18}$ Clusters *J. Phys. Chem. C* **2013**, *117*, 20867−20875

[21] Zhao, L.; Jensen, L.; Schatz, G. C. *J. Am. Chem. Soc.* **2006**, *128*, 2911−2919

[22] Barcaro, G.; Sementa, L.; Fortunelli, A.; Stener, M. Optical Properties of Silver Nanoshells from Time-Dependent Density Functional Theory Calculations *J. Phys. Chem. C*, **2014**, *118*, 12450–12458

[23] Bernadotte, S.; Evers, F.; Jacob, C. R. Plasmons in Molecules *J. Phys. Chem. C* **2013**, *117*, 1863−1878

[24] Piccini, G. M.; Havenith, R. W. A.; Broer, R.; Stener, M. Gold Nanowires: A Time-Dependent Density Functional Assessment of Plasmonic Behavor *J. Phys. Chem. C* **2013**, *117*, 17196 – 17204

[25] Reimers, J. R.; Wang, Y.; Cankurtaran, B. O.; Ford, M. J. *J. Am. Chem. Soc.* **2010**, 132, 8378–8384